Double slot micro ring resonators with inner wall angular gratings as ultra-sensitive biochemical sensors

WEIQING CHENG,[1,*] XIAO SUN,[1] SHENGWEI YE,[1] BOCHENG YUAN,[1] JICHUAN XIONG,[2] XUEFENG LIU,[2] YIMING SUN,[1] JOHN H. MARSH,[1] AND LIANPING HOU[1]

[1]*James Watt School of Engineering, University of Glasgow, Glasgow G12 8QQ, UK*
[2]*School of Electronic and Optical Engineering, Nanjing University of Science and Technology, Nanjing 210094, China*
[*]*w.cheng.2@research.gla.ac.uk*

Abstract: We simulate and demonstrate experimentally an inner-wall grating double slot micro ring resonator (IG-DSMRR) with a center slot ring radius of only 6.72 µm based on the silicon-on-insulator platform. This novel photonic-integrated sensor for optical label-free biochemical analysis boosts the measured refractive index (RI) sensitivity in glucose solutions to 563 nm/RIU with the limit of detection value being 3.7×10^{-6} RIU (refractive index units). The concentration sensitivity for sodium chloride solutions can reach 981 pm/%, with a minimum concentration detection limit of 0.02%. Using the combination of DSMRR and IG, the detection range is enlarged significantly to 72.62 nm, three times the free spectral range of conventional slot micro ring resonators. The measured Q-factor is 1.6×10^4, and the straight strip and double slot waveguide transmission losses are 0.9 dB/cm and 20.2 dB/cm, respectively. This IG-DSMRR combines the advantages of a micro ring resonator, slot waveguide, and angular grating and is highly desirable for biochemical sensing in liquids and gases offering an ultra-high sensitivity and ultra-large measurement range. This is the first report of a fabricated and measured double-slot micro ring resonator with an inner sidewall grating structure.

1. Introduction

Biomedical detection sensors have wide applications in areas such as biomedical research, medical diagnostics, healthcare, and environmental monitoring. Label-free optical sensing is widely used as it is a relatively simple and low-cost approach compared with traditional label-based detection strategies [1].

In photonic integrated circuits (PICs), silicon-on-insulator (SOI) platforms have been recognized as favorable candidates due to their compatibility with well-established metal-oxide-semiconductor (CMOS) fabrication technologies. SOI structures have a high refractive index (RI) contrast, with strong optical mode field confinement enabling tight bending designs (down to a 1.5 µm bend radius, close to the theoretical limit) [2]. Label-free optical sensing devices based on the SOI platform have been widely studied, including Mach–Zehnder interferometer sensors [3], Fabry–Perot resonance sensors [4], microring/microdisk resonator sensors [5,6,7,8], and grating sensors [7,8,9].

SOI-based micro ring resonator (MRR) structures have previously been combined with waveguide grating elements to create filters [10], single wavelength micro ring mirrors [11], single mode lasers [12], optical vortex beam emitters [13], and nonlinear sensing devices [14]. For MRR sensors, two typical interrogation approaches, intensity interrogation, and wavelength

interrogation have been utilized [15]. The former suffers from a narrow detection range and unstable accuracy. Wavelength interrogation has therefore become a popular detection method, meeting the requirements of a large detection range and easy-to-identify sensing.

Specifically, for MRR sensing using the wavelength shift, if the refractive index change is sufficiently large, the resonant wavelength can be shifted over the entire free spectral range (FSR) of the MRR device. The measurement range of a wavelength shift-dependent MRR device is therefore limited by its FSR. Schemes such as Mach–Zehnder interferential coupled micro rings [16], serially coupled double MRRs [17], grating-coupled silicon MRRs [18], and angular grating (AG) MRRs [19] have been proposed to enlarge the FSR. Although these schemes can enlarge the FSR, their sensitivities are lower than those of multi-slot micro ring resonator (SMRR) schemes. Traditional single-strip waveguide MRR bulk sensitivity is around 70 nm/RIU [20]. Even using a specially designed quasi-TM MRR, the maximum bulk sensitivity of a traditional strip waveguide MRR sensor based on wavelength shifting is only 270 nm/RIU [21], while SMRR sensing structures on SOI can enhance the light–analyte interaction with experimentally demonstrated sensitivities up to 298 nm/RIU (5 μm bend radius) [22], and 476 nm/RIU (30 μm bend radius) [23].

In this paper, we present a compact label-free optical sensor with a combination of an inner sidewall grating and a double slot micro ring resonator (IG-DSMRR). An MRR design using angular grating and one slot waveguide with a large measurement range (84.5 nm) and high bulk sensitivity (559.5 nm/RIU) has previously been reported but the results were simulations [24]. Furthermore, the design had no input and output grating couplers, so it would not be suitable for practical sensing. Our simulation and experiment results show that, based on the SOI platform, a DSMRR combined with a Bragg angular grating structure can have a detection range more than three times that of a conventional MRR combined with a sensitivity which is more than that of an SMRR. Lumerical FDTD solutions are utilized to simulate and optimize the structural parameters to enhance the sensing performance of the device. The measured refractive index (RI) sensitivity can reach 563 nm/RIU with a Limit of Detection (LOD) value of 3.7×10^{-6} RIU. The concentration sensitivities of sodium chloride could reach 981 pm/% with a minimum concentration detection limit of 0.02%, and a large measurement range of 72.62 nm. The IG-DSMRR device has a high Q-factor of 1.6×10^4, a straight strip waveguide transmission loss of only 0.9 dB/cm and a double slot waveguide transmission loss of 20.2 dB/cm. This is the first demonstration of a fabricated IG-DSMRR based on the SOI platform offering a large detection range with high sensitivity.

2. Structure design and operation principle

2.1. Structure design

The SOI wafer epilayer and the three-dimensional (3D) schematic of the proposed sensing device are illustrated in Fig. 1(a), and the detailed design parameters of the IG-DSMRR are shown in Fig. 1(b). The SOI wafer has a 220 nm top silicon layer and a 2 μm buried oxide (BOX) layer on a 675 μm thick silicon substrate. The structure contains focused grating couplers at the ends of the waveguides to couple the device optically to cleaved single mode fibers (SMF), and an optimized "W" shaped branch tapered coupler is used to couple light between the strip waveguides and slot waveguides. The inner wall of the MRR has a grating structure to enable sensing with high sensitivity over a large detection range. Homogeneous sensing is implemented in this sensing structure, so the IG-DSMRR part of the device is immersed in aqueous solutions in both simulation and experiment. Pure water was chosen as the top cladding in the process of determining the geometric parameters of waveguides. This homogeneous sensing case can be easily extended to surface sensing applications by modeling the device with a thin adsorbed analyte for the top cladding. The bend radius (R) of the DSMRR is the distance between the center of the rings and the inner wall of the middle ring, which is designed to be 6.72 μm. The

gap width between the bus and the ring waveguide is denoted as W_{gap} (200 nm) and the ring and bus waveguide have the same slot width named W_{slot}. The strip waveguide width W_{strip} is 630 nm and the bus and ring width W and the slot width W_{slot} are set to 210 nm and 100 nm respectively, which results in a high mode confinement factor and extremely strong electric field enhancement in the slots. The etched IG has an azimuthal period (Λ) of 1.199 μm and duty cycle, or filling factor (*FF*) (ratio of silicon block l_g to the period Λ) of 96%, and the corrugation depth of the grating H_g is 24 nm. The propagation of the optical fields in the bus and ring slots is shown in Fig. 1(c). Here E_1^+, E_2^+, E_3^+ and E_4^+ represent the input and the output optical field amplitudes with respect to the ring coupling point in bus double slots and ring double slots, and E_1^-, E_2^-, E_3^- and E_4^- represent the reflected optical field amplitudes in the corresponding positions.
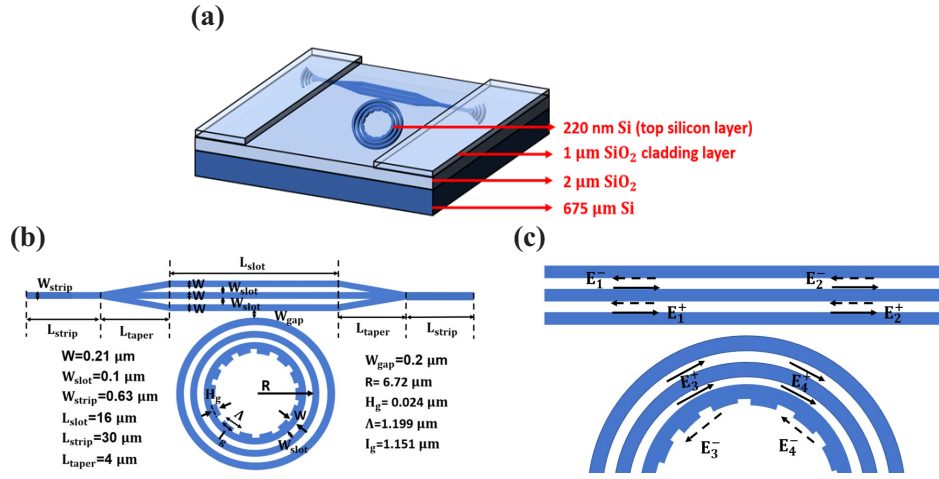

Fig. 1. (a) Schematic structure of the IG-DSMRR. (b) Design parameters of the IG-DSMRR structure. (c) Propagating optical fields in the bus and bent double slots.

2.2. Operation principle

The resonance equation of the DSMRR can be expressed as:

$$Ln_{eff} = m\lambda_{res}, m = 1, 2, 3 \ldots \tag{1}$$

where $L = 2\pi R$ is the perimeter of the ring, n_{eff} is the effective refractive index of the DSMRR waveguide, m (positive integer) is the azimuthal resonant order, and λ_{res} is the resonant wavelength.

The input and output ports of the IG-DSMRR device are symmetric, so the optical path is reversible. The transmission matrix of incident and reflected optical fields between the bus waveguide and ring waveguide is expressed separately as:

$$\begin{pmatrix} E_2^+ \\ E_4^+ \end{pmatrix} = \begin{pmatrix} \tau & j\kappa \\ j\kappa & \tau \end{pmatrix} \begin{pmatrix} E_1^+ \\ E_3^+ \end{pmatrix} \tag{2}$$

$$\begin{pmatrix} E_1^- \\ E_3^- \end{pmatrix} = \begin{pmatrix} \tau & j\kappa \\ j\kappa & \tau \end{pmatrix} \begin{pmatrix} E_2^- \\ E_4^- \end{pmatrix} \tag{3}$$

where, κ and τ are the amplitude coupling and transmission coefficients. When coupling loss can be ignored, the relation between them is described as:

$$\kappa^2 + \tau^2 = 1 \tag{4}$$

The transmission matrix of the IG [25] is written as:

$$
\begin{pmatrix} E_3^+ \\ E_4^- \end{pmatrix} = e^{-\alpha L} \cdot e^{j\beta L} \cdot S \begin{pmatrix} E_3^- \\ E_4^+ \end{pmatrix} = e^{-\alpha L} \cdot e^{j\beta L} \cdot \begin{pmatrix} -jre^{-j\varphi} & t \\ t & jre^{-j\varphi} \end{pmatrix} \cdot e^{j\phi} \begin{pmatrix} E_3^- \\ E_4^+ \end{pmatrix} \tag{5}
$$

where S is the scattering matrix of the IG, and α and β are the transmission loss coefficient and propagation constant, respectively. When the transmission loss α is negligible ($\alpha = 0$). The r and t, in the S matrix, are the reflection and transmission coefficients of the IG which satisfy:

$$
r^2 + t^2 = 1 \tag{6}
$$

Combining Eq. (2)-(6), and setting $E_2^- = 0$ (no reflected signal from the output port), the transfer function of IG-DSMRR is derived as:

$$
A = \left| \frac{E_2^+}{E_1^+} \right|^2 = \frac{[t(1 + \tau^2) - 2\tau \cos(\beta L + \phi)]^2}{(1 - t^2)[(1 + \tau^2)^2 - 4\tau^2] + [t(1 + \tau^2) - 2\tau \cos(\beta L + \phi)]^2} \tag{7}
$$

Here A is the intensity transmission, which is usually expressed in the logarithmic form:

$$
T(\lambda) = 10\log_{10}(A) \tag{8}
$$

To decide the wavelength selectivity, we calculate the fundamental mode in an angular grating using the mode analysis, the effective indices (n_{avr}) of the fundamental modes and reflection condition of Bragg grating are calculated as below [19]:

$$
n_{avr}^2 = FF \cdot n_{eff1}^2 + (1 - FF) \cdot n_{eff2}^2 \tag{9}
$$

$$
2\lambda_B = 2n_{avr}\Lambda \tag{10}
$$

where n_{eff1} and n_{eff2} are the wavelength-dependent effective indices of the ring waveguide at section with and without inner wall grating, FF is the filling factor of the IG as denoted above, and λ_B is the Bragg wavelength. The operating principle of the designed sensor is demonstrated in Fig. 2, in which the spectral responses of the DSMRR, IG, and IG-DSMRR are described. The optical transmission can be regarded as two filtering processes. The light in the bus waveguide is first filtered by DSMRR, and then the resonant light is filtered by the IG. The DSMRR and IG have the same resonant wavelength (near 1550 nm) as the main resonant peak of the IG-DSMRR, and other resonances of the DSMRR are filtered by the IG. The IG-DSMRR with the wavelength-selective characteristic is not restricted by the FSR of DSMRR. In the second filtering stage, certain side modes can be effectively suppressed by optimizing the corrugation depth of the IG. The side-mode suppression ratio (SMSR) is used to describe the level of suppression.
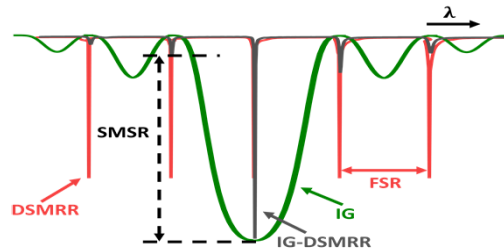

Fig. 2. Demonstration of the operating principle of the IG-DSMRR.

3. Simulation

3.1. Modeling considerations

The simulation of this IG-DSMRR sensor was conducted and optimized using Finite Difference Time Division (FDTD) and MODE solutions software of Lumerical Inc. (Vancouver, BC, Canada) [26]. Under the effective indices simulation of DSMRR and IG, an operation wavelength is preferable to be fixed near 1550 nm. The grating couplers were simulated using Lumerical 2D Finite Difference Eigenmode (FDE) to optimize the grating pitch, duty cycle, and fiber coupling position. Then using 3D FDTD methods to optimize the final fiber position based on 3D simulation to achieve the highest coupling efficiency. The ''W'' shape strip-to-slot waveguide coupler is also simulated using the 3D FDTD method. The IG-DSMRR structure was simulated using a variational FDTD simulation approach to calculate the transmission spectral responses of the sensor. A tunable laser of TE-like (the fundamental mode TE0) was injected into the double slot bus waveguide. The mode field distribution was calculated by using a Finite Difference Eigenmode (FDE) solver. In the process of the structure parameter optimization, pure water is chosen as the top cladding. The Q-factor (Q) can be calculated as the ratio of the resonance wavelength (λ_{res}) and full width at half maximum (FWHM) of the transmission spectrum as the expression:

$$Q = \frac{\lambda_{res}}{FWHM} \tag{11}$$

The concentration sensitivity [27] of the optical sensor can be defined as:

$$S_C = \Delta\lambda_{res}/\Delta C \tag{12}$$

where ΔC and $\Delta\lambda_{res}$ are the variations in the sample (gas or liquid) concentration and resonant wavelength, respectively. This concentration sensitivity means the resonant wavelength shift induced by 1% mass concentration change.

For comparative purposes, the universal RI sensitivity can be written as:

$$S_V = \Delta\lambda_{res}/\Delta n \tag{13}$$

where Δn is the RI variation of the aqueous solution. This sensitivity, with the unit of nm/RIU, means the resonant wavelength shift induced by unit change in the RI.

The surface RI sensitivity (S_s) is a measure of the wavelength shift per unit change in refractive index within the first few tens of nanometers (adlayer thickness) above the waveguide and is important in biosensing applications [28]:

$$S_S = \frac{\Delta\lambda_{res}}{\Delta t_{ad}} = \frac{\lambda_{res}}{n_g} \left(\frac{\partial n_{eff}}{\partial t_{ad}}\right) \tag{14}$$

where n_g is the group index, t_{ad} is the uniform thickness of the adsorbed molecule layer with refractive index n_{ad}. For most proteins, the refractive index is about $n_{ad} = 1.48$ [28].

The limit of detection (LOD) is another widely used parameter to evaluate the sensing capability of a device, and is defined as the resonance wavelength resolution 3σ divided by the sensitivity (S_C or S_V), where σ is the standard deviation of the resulting spectral variation and can be calculated using the method in [29]:

$$LOD = 3\sigma/S_C \text{ or } LOD = 3\sigma/S_V \tag{15}$$

To demonstrate the bulk sensing characteristics of the IG-DSMRR, sodium chloride (NaCl) and D-glucose ($C_6H_{12}O_6$) were used as samples. Concentrations changes (mass%) of sodium

chloride and glucose results in the RI changes are calculated using a third-order polynomial fit as [30,31]:

$$n = Aw^3 + Bw^2 + Cw + D \qquad (16)$$

where w is the weight fraction, A, B, C and D are the parameters of a polynomial fit, with the values for glucose and sodium chloride solutions listed in Table 1.

Table 1. Parameters for refractive indexes of solutions

	NaCl	Glucose
w	0-0.25	0-0.80
A	-0.0800	0.0330
B	0.0740	0.0456
C	0.1620	0.1416
D	1.3162	1.3166

3.2. Simulation results

Introducing slots into a common bus waveguide can lead to strong confinement of the quasi-TE mode in the slot regions. This strong confinement can enhance light-matter interaction and potentially improve the sensitivity of the sensor. The width of the slot must be designed carefully since too wide a slot will weaken the electrical strength in the slot region while too narrow a slot will prevent biological molecules from entering the slot region. Here, the width of the slot region is selected to be 100 nm. The mode field distribution of a straight double slot waveguide and of the bent double slot waveguide in the ring are shown in Fig. 3(a) and Fig. 3(b) respectively. The straight double slot waveguide has relatively symmetric electric field patterns in the two slots, while the bent double slot waveguide has an asymmetric distribution with the inner slot having a higher electric field strength than the outer one. High confinement of the TE mode in the slots 37.2% and 37.8% for the straight waveguide and 38.7% and 41.2% for the bent slot waveguide and an intensified electric field were realized within the slot region for the applied geometry in both bus and bent waveguide. On the other hand, the strong E-field confinements in the slots also cause more losses due to more sidewall scattering and water absorptions as compared with conventional strip waveguides. In the non-sensing state, the measured propagation loss of a straight single strip waveguide in air is 0.9 dB/cm, close to the result in [32] which used similar fabrication processes and same waveguide width. The measured propagation loss of a straight double slot waveguide in air (including sidewall scattering loss) is 20.2 dB/cm (see Section 4.3. Experimental results below). The water absorption loss is 47.5 dB/cm at a wavelength of 1.55 µm [33]. In the sensing state, the estimated propagation loss of the double slot waveguide is therefore about 20.2 dB/cm + (0.372 + 0.378) × 47.5 dB/cm = 55.8 dB/cm.
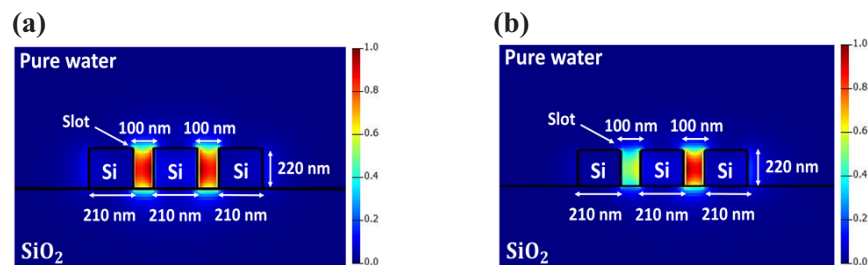

Fig. 3. (a) Electric field distribution of the bus double slot waveguide. (b) Electric field distribution of the bent double slot waveguide.

An optical label-free sensor must have a high sensitivity to be of practical use. The extinction ratio (*ER*), defined as the ratio between on-resonance and off-resonance transmission, and the *Q*-factor of the IG-DSMRR are also two key parameters. To increase the *Q*-factor, it is important to reduce the resonator losses. The losses of the IG-DSMRR mainly arise from the intrinsic propagation loss in the silicon straight slot waveguide, the bus-ring coupling loss, the bending loss, and scattering loss. The scattering loss is mainly caused by the IG and waveguide sidewall roughness arising from the fabrication process. So in the IG-DSMRR, the coupling loss, bending loss, and scattering loss of IG and the smoothness of the waveguide sidewall in fabrication dominate the total loss, and a small bus to ring waveguide coupling distance can effectively decrease the coupling loss. Taking into account the trade-off between the coupling efficiency from the double slot straight waveguide to the double slot ring resonator and the reactive ion etching (RIE) lag effect in fabrication, the coupling distance W_{gap} between the bus waveguide and ring waveguide was chosen to be 200 nm. The focused SOI grating coupler was optimized for use with a cleaved SMF angled at 10° from vertical. The optimized grating pitch *P* is 671 nm, the duty cycle is 39.9%, and the grating height h_e is 100 nm for operation at a central wavelength of 1550 nm.

The simulation of the IG-DSMRR is based on the parameters presented in Fig. 1(b) which were chosen to optimize the sensing performance. The electric field distribution of the IG-DSMRR structure is shown in Fig. 4(a). The simulated transmission spectra of the designed IG-DSMRR and fabricated IG-DSMRR are shown in Fig. 4(b). The relatively low *ER* (<9 dB) may be due to the coupling efficiency κ between the bus and the ring waveguide being only 1.40% (see Section 4.3. Experimental results below), and the increased sidewall scattering losses of the double-slot ridge waveguides and the IG structure. However, there is a trade-off between the *Q*-factor and the *ER* because a low value of κ corresponds to a high *Q*-factor and lower *ER* [34]. The resonant peak of the designed IG-DSMRR is at 1545 nm, and the resonant peak for the structure with the fabricated parameters is slightly blue shifted to 1543 nm because the grating height of the fabricated inner wall is around 210 nm, smaller than the designed value of 220 nm. When the hydrogen silsesquioxane (HSQ) resist mask is removed following the etch to define the ridge waveguide and IGs, the remaining (unetched) 10 nm thick layer of Si can be used as a wet etch stop layer (see device fabrication in below section 4.1).
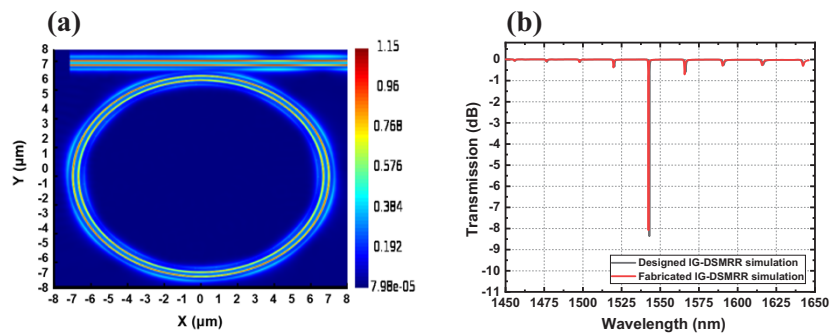

Fig. 4. (a) The electric field distribution of the IG-DSMRR. (b) The simulated transmission spectrum of the IG- DSMRR for the designed IG height of 220 nm (black curve) and the fabricated IG height of 210 nm (red curve).

An optimized "W" shaped branch tapered coupler was used to couple light between the strip waveguide and the slot waveguide also enhance the transmission intensity to increase *ER* [35]. The design and parameters of the "W" shaped branch tapered coupler are shown in Fig. 5(a), and the electric field distribution associated with the coupler is shown in Fig. 5(b).
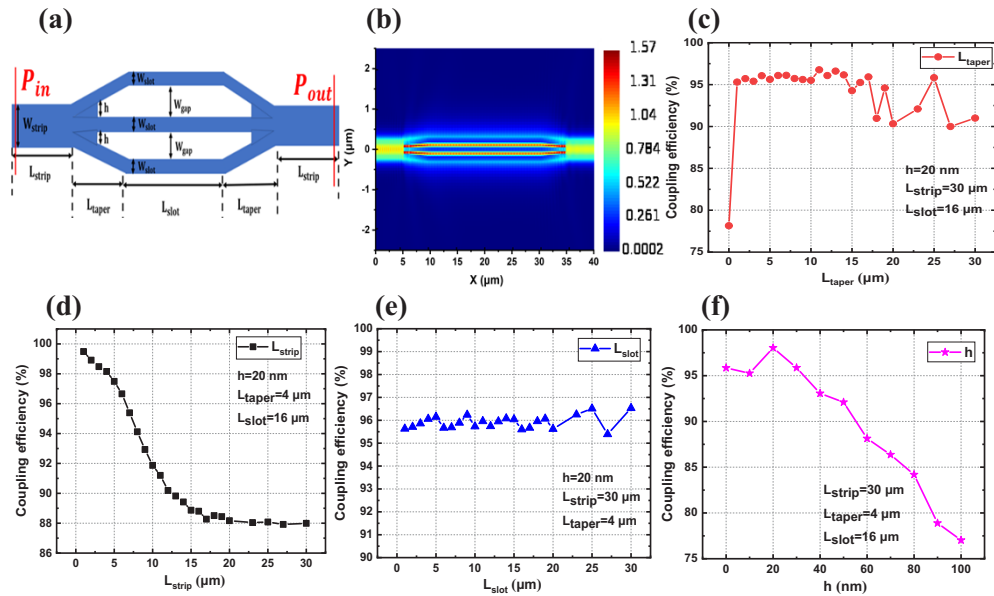
Fig. 5. (a) The "W" shaped branch tapered coupler design. (b) The electric field distribution in the "W" shaped branch tapered coupler. The coupling efficiency as a function of (c) strip waveguide length, (d) taper waveguide length, (e) slot waveguide length, and (f) h value.

The optimization of the "W" shaped branch tapered coupler is based on the following parameters: the strip waveguide length L_{strip}, the taper waveguide length L_{taper}, the slot waveguide length L_{slot}, the h value arising from limits in the fabrication resolution. The simulated coupling efficiencies of structures with different L_{strip}, L_{taper}, L_{slot}, and h values are shown in Fig. 5(c), (d), (e), and (f), respectively. The coupling efficiency decreases for longer L_{strip} and larger h values, and fluctuates as L_{taper} and L_{slot} are increased. Based on these simulation curves, the optimized parameters were selected as $L_{strip} = 30 \,\mu\text{m}$, $L_{taper} = 4 \,\mu\text{m}$, $L_{slot} = 16 \,\mu\text{m}$, and $h = 20 \,\text{nm}$. The coupling efficiency of the optimized coupler can reach 96%.

After adding this optimized "W" shaped branch tapered coupler to the IG-DSMRR, the simulation was performed again to confirm the sensing performance. The transmission spectra with and without the taper coupler are shown in Fig. 6(a). There is a measured principal resonant peak at 1543 nm. The transmission intensity in the spectrum is slightly enhanced which brings a higher *ER* and confirms the optimized taper coupler will not affect the transmission spectrum of the IG-DSMRR. The simulated transmission spectra for different concentrations of glucose and sodium chloride as the top cladding mediums are shown in Fig. 6(b) and Fig. 6(c), respectively. The RI of the cladding solution on the top of the sensor influences the field of the optical mode, which results in a change in the effective index and a shift in the resonant frequencies of the MRR. Here, the strong resonant optical field inside the slots plays a crucial role in the sensing process. The simulated surface sensitivity S_s is 0.219 nm/nm as shown in Fig. 6(d).
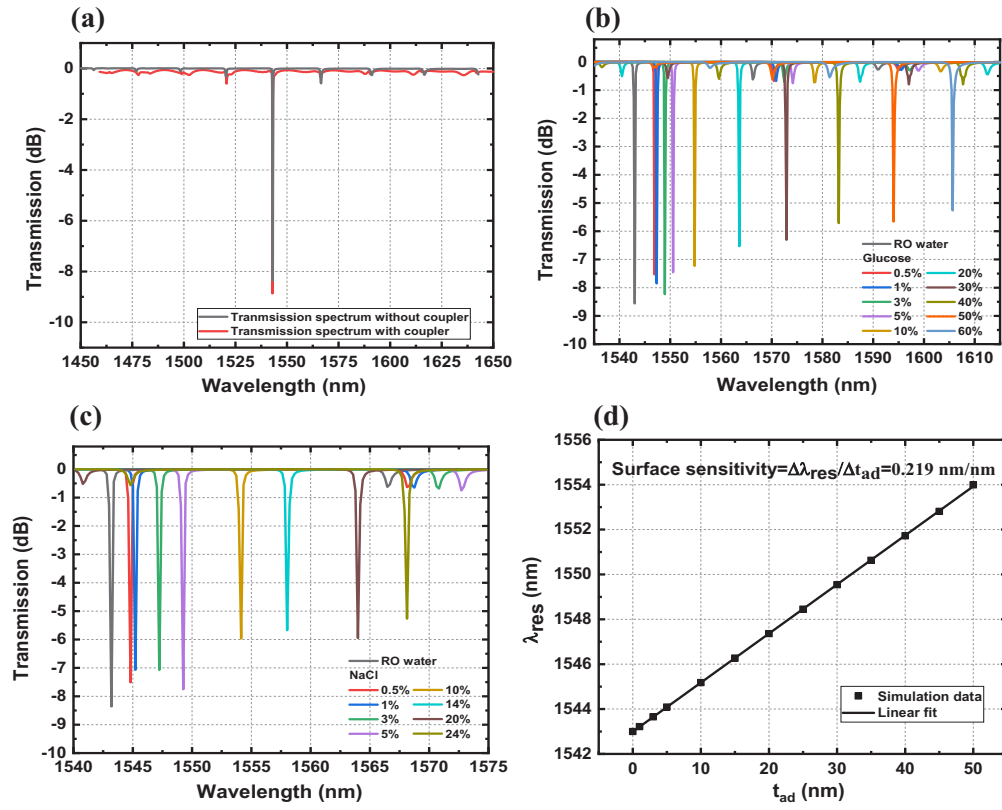
Fig. 6. (a) Simulated transmission spectra of IG-DSMRR without (black curve) and with tapered coupler (red curve). (b) Simulated transmission spectra for different concentrations of glucose solutions. (c) Simulated transmission spectra for different concentrations of sodium chloride solutions. (d) Simulated surface sensitivity S_s.

4. Experiment

4.1. Device fabrication

The SOI wafer structure was shown in Fig. 1(a). The fabrication process consisted of 5 main steps, as shown in Fig. 7.
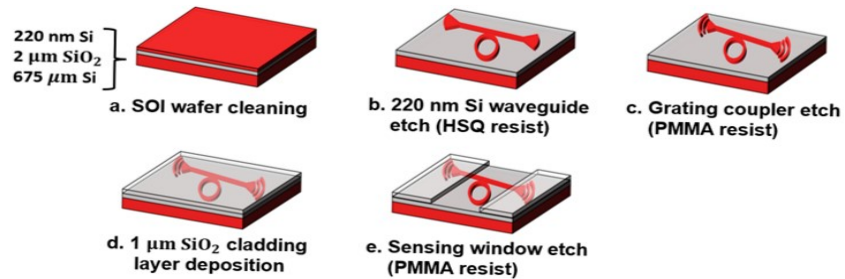

Fig. 7. Fabrication steps of the device.

    The fabrication process uses three etching steps to create the waveguides and ring resonators, the grating couplers, and the sensing windows. First, the SOI substrates were cleaned by
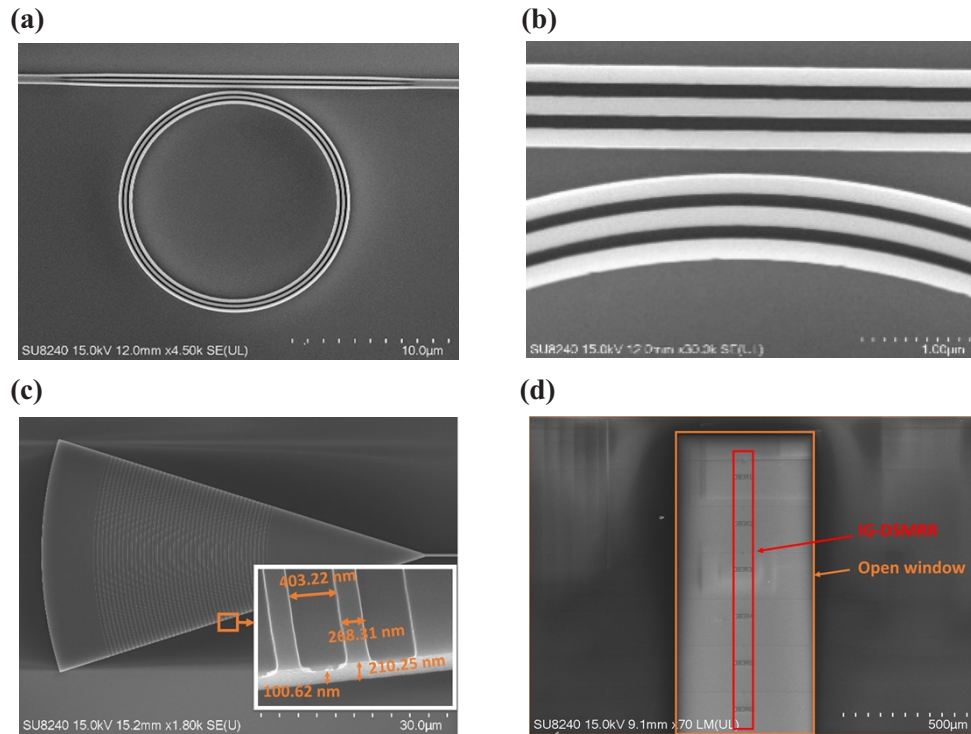
Fig. 8. SEM images of (a) the IG-DSMRR. (b) zoomed bus, ring waveguides, and the inner sidewall grating. (c) the grating coupler, and the inset shows the grating period of 672 nm and dry etched grating height of around 110 nm. (d) the dry-etched open window for a series IG-DSMRRs.

submerging in acetone, isopropanol (IPA) and RO water. Second, an electron beam lithography (EBL) resist 1:3 HSQ: MIBK film was spin-coated and baked at 90 ∘C. After that, EBL (Raith EBPG 5200) was used to define all the waveguides and the IGs. Then, the exposed samples were developed with 25% tetramethylammonium hydroxide (TMAH). After that, the topsilicon patterns of the ridge waveguides and IGs were dry etched using an inductively coupled plasma (ICP) STS 100 tool with a gas flow of SF_6/C_4F_8 (30:90 sccm). Third, another EBL resist layer, of polymethyl methacrylate (PMMA, AR-P 642 200 k Anisole 12% PMMA), was spin-coated and the samples were baked using a hotplate at 180 ∘C. Then, EBL was carried out to the input and output grating couplers, and the exposed samples were developed with an IPA/MIBK (2.5:1) solution. Then, the silicon layer of the grating coupler was dry etched using an ICP STS 100 system with flow rates of SF_6/C_4F_8 (30:90 sccm). Fourth, a 1 μm silicon oxide layer was deposited on the whole sample using plasma-enhanced chemical vapor deposition (PECVD) to form a cladding layer to increase the coupling efficiency of the grating coupler with a SMF. Fifth, a 1-μm-thick SiO_2 window over the ring resonator section was opened by using three PMMA (AR-P 642 200 k Anisole 15% PMMA) resist layers and dry-etching in CHF_3/Ar (25/18 sccm). Here we note that the EBL resist thicknesses, EBL doses and beam step size (BSS) had been optimized previously. The top view scanning electron microscope (SEM) picture of the fabricated IG-DSMRR device is shown in Fig. 8(a) and (a) zoomed SEM picture of the inner sidewall grating is shown in Fig. 8(b). The fabricated grating coupler is shown in Fig. 8(c), from which the period and duty cycle are 672 nm and 39.9% with an etch depth of 110 nm. These parameters are close to the designed period and duty cycle (671 nm and 39.9%), the differences being due to
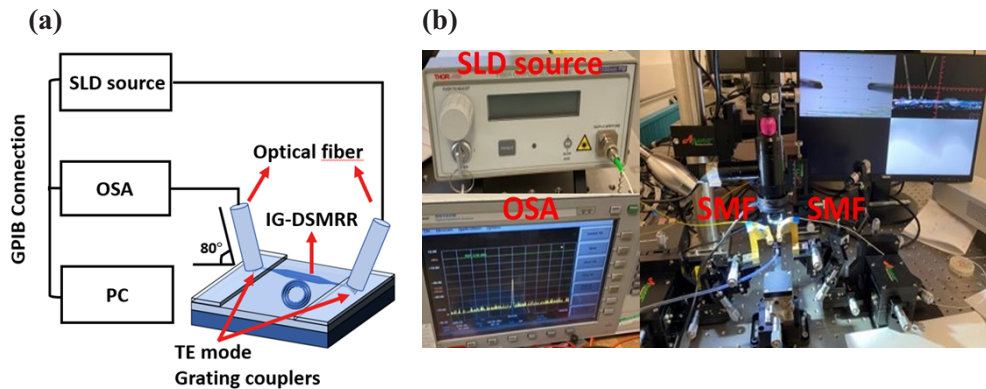
Fig. 9. (a) Experimental setup for measuring IG-DSMRR. (b) Photograph of the measurement setup, in which there is an SLD, OSA, input and output SMFs, alignment stage, and two displays.

the fabrication errors which result from proximity effects in EBL and side wall etching during the ICP-RIE process [36]. The open window on the ring resonator for high-sensitivity sensing is shown in Fig. 8(d).

4.2. Measurement setup

In the experimental setup, a Super Luminescent Diode (SLD, THORLABS S5FC1005P - PM Benchtop SLD Source), with a central wavelength of 1550 nm, maximum output power of 22 mW, and a 3 dB bandwidth of 50 nm was used as the light source to measure the spectral response. The experimental setup is shown in Fig. 9(a) and Fig. 9(b). The input and output beams in TE mode were connected to the IG-DSMRR sensors via a 10 μm core cleaved SMF with 10° input and output angles through the grating couplers (GCs). An optical spectrum analyzer (OSA) with a resolution bandwidth of 0.06 nm was connected to the output SMF to measure the transmission spectrum of the IG-DSMRR. To measure the sensitivity of the sensor to different RIs, sample liquids were dropped on the sensing part as shown in Fig. 9(a). To obtain measurement data swiftly, particularly important for fast evaporation solvents such as acetone, an automated measurement system using LabVIEW software based on the general purpose interface bus (GPIB) connection was employed.

4.3. Experimental results

In the experiments, the coupling efficiency of the grating coupler, the transmission loss of the straight SOI waveguide, and the transmission spectra of the IG-DSMRR with different concentrations of glucose and sodium chloride solutions were measured. The simulated and measured coupling efficiencies as a function of wavelength of the output grating coupler are shown in Fig. 10(a). The central wavelength and coupling efficiency of the simulated grating coupler based on the fabricated parameters are 1548 nm and 38% respectively. For the real measured grating coupler, the central wavelength and coupling efficiency are 1540 nm and 34% respectively. The differences in the central wavelength and coupling efficiency may be due to deviations in the tilt angle of the output SMF. The transmission spectra of the simulated and measured IG-DSMRR are shown in Fig. 10(b). There is a measured principal resonant peak at 1547.76 nm, which can be tuned from 1450 nm to 1650 nm. Nearly 5-nm redshift in the resonant peak compared with the simulation result in Fig. 6(a) may be due to the fabrication errors of the IG period and FF. The distance between the main resonant peak and its right-third subsidiary peak is denoted as the quasi-FSR. In the spectrum, the quasi-FSR of the IG-DSMRR is 72.62 nm,
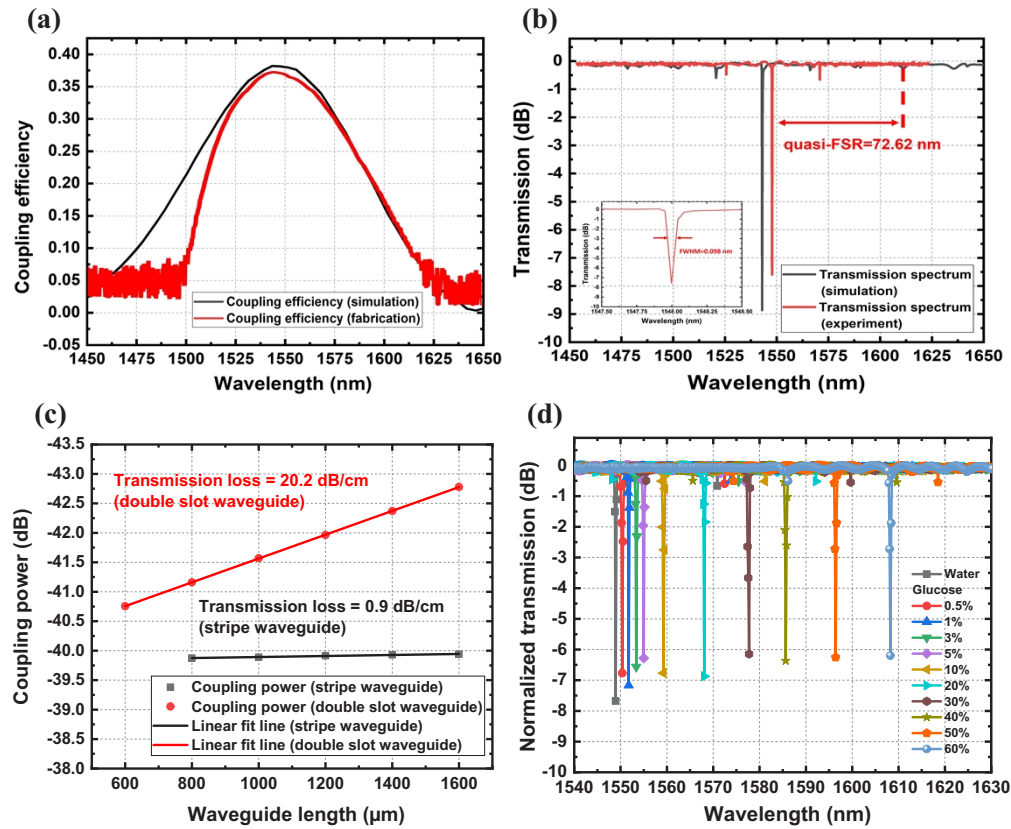
Fig. 10. (a) Coupling efficiency of the simulated (black line) and fabricated (red line) focused grating coupler. (b) Transmission spectra of the simulated (black line) and measured (red line) IG-DSMRR. (c) Coupling power of the strip and double slot SOI waveguide vs waveguide length. (d) Measured transmission spectra for different concentrations of glucose solution.

compared to the FSR of a conventional SMRR of 20.44 nm. This magnification of the detection wavelength range can be defined using Eq. (17) to give a measure of the degree of broadening of the detection range:

$$A_{EF} = \frac{quasi - FSR}{FSR} \qquad (17)$$

The calculated enlargement factor of this device is up to 3.55, hence the operating range of the proposed IG-DSMRR is expanded significantly. The large FSR of the IG-DSMRR also brings advantages. Conventional MRRs can only detect glucose concentrations below 20% [34], while the large quasi-FSR of the IG-DSMRR allows higher concentrations to be measured without ambiguity. The Q-factor can be calculated from Eq. (11): from the transmission spectrum the resonant wavelength is 1547.76 nm and the FWHM is 0.098 nm, giving the Q-factor as 1.6×10^4. The measured coupling efficiency κ between the bus and the ring waveguide is about 1.40%. The measured transmission losses of the straight strip and double slot SOI waveguides are shown in Fig. 10(c) and are calculated from the coupled output power using different lengths of waveguides. The transmission loss is 0.9 dB/cm for the straight strip SOI waveguide, and 20.2 dB/cm for the straight double slot waveguide with air cladding. Under sensing condition, the calculated propagation loss of straight double slot waveguide is 55.8 dB/cm as noted above.
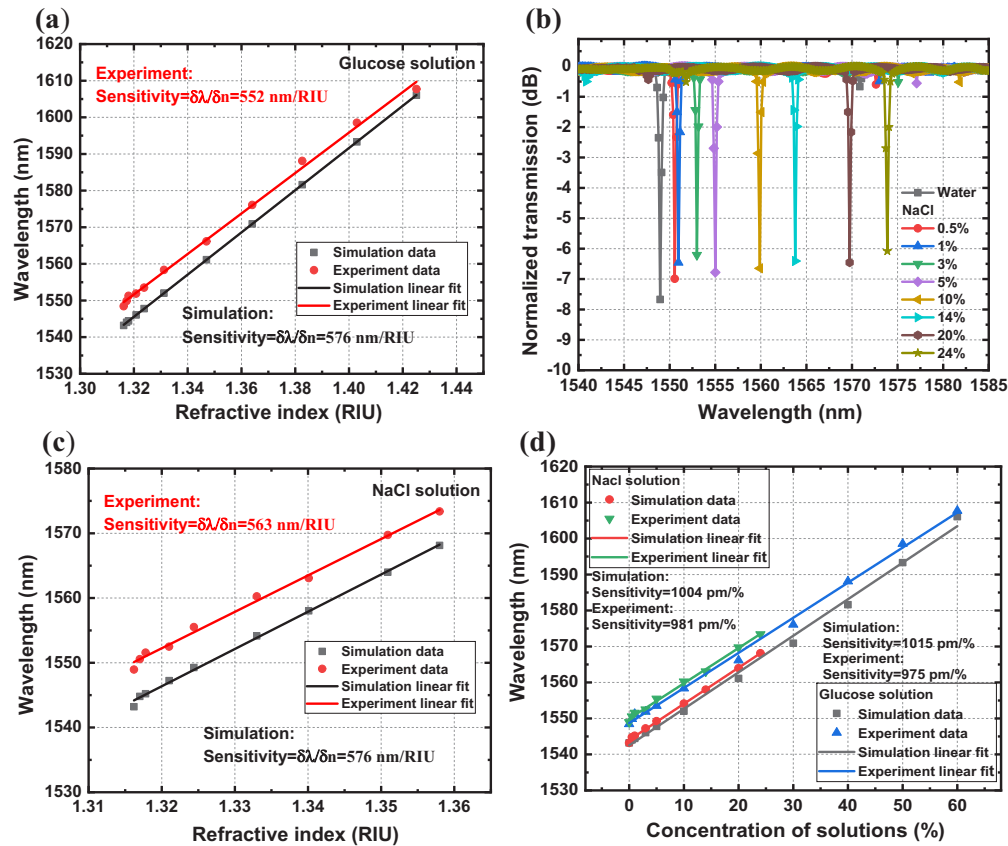
Fig. 11. (a) The RI sensitivity of IG-DSMRR of simulation (square black line) and experiment (red dot line) (glucose). (b) measured transmission spectrum of different concentrations of NaCl solution. (c) The RI sensitivity of IG-DSMRR of simulation (square black line) and experiment (red dot line) (NaCl). (d) The simulation and experiment concentration sensitivity of IG-DSMRR for glucose and NaCl solutions respectively.

The transmission spectra for different concentrations of glucose and sodium chloride are shown in Fig. 10(d) and Fig. 11(b) respectively. Samples with different concentrations of glucose and sodium chloride were dropped onto the ring resonator. The resonant peak starts at 1547.76 nm and as the concentration of solute is increased, the waveguide effective index increases and the resonant peak in the spectrum is red shifted. The wavelength sensitivity can be calculated from the changes in the resonance and in the refractive index. The simulated and measured sensitivities of the device to glucose and sodium chloride concentration are shown in Fig. 11(a) and Fig. 11(c) respectively. The simulated bulk sensitivities to glucose and sodium chloride are both 576 nm/RIU, while the measured structure bulk sensitivities are 552 nm/RIU and 563 nm/RIU respectively. The achieved bulk sensitivity is more than two times that of optimized designed single strip SOI-based quasi-TM MRRs [21]. It is also higher than that of reported SMRRs [22,23]. The measured LOD values related to these sensitivities are 3.6×10^{-6} RIU and 3.7×10^{-6} RIU respectively. The concentration sensitivities are also shown in Fig. 11(d), where the simulated concentration sensitivities are 1015 pm/% and 1004 pm/% for glucose and sodium chloride solutions respectively, with the experiment concentration sensitivities being 975 pm/% and 981 pm/% respectively. The corresponding measured concentration LOD values are both 0.02%. Experimentally, the central coupling wavelength of the grating couplers and the

transmission peak of the IG-DSMRR were 10 nm blue shifted and 5 nm red shifted respectively compared with the simulation results, which may be because of fabrication errors and the analytes RIs fluctuations between the reference and the experiment.

It should be noted that due to the lack of an accurate tool to measure the protein layer thickness t_{ad}, the measured surface sensitivity Ss could not be determined. However, we estimate that the experimental Ss value should be close to the simulated value of 0.219 nm/nm because the measured bulk sensitivity is nearly the same as that of the simulation.

5. Conclusions

In conclusion, compact and highly sensitive IG-DSMRR sensors were developed. This sensor is a combination of a double slot micro ring resonator and inner sidewall angular grating. In contrast to previous work reporting a similar double slot waveguide configuration, this structure with inner wall grating is designed to have only one resonant peak with other peaks suppressed. As a result, the new design offers the combination of high sensitivity and large detection range in a compact size as 6.72 μm center radius non-suspended ring resonator structure. After designing and modeling, devices were fabricated using high-precision EBL and dry etching to realize a slot waveguide ring resonator with microns scale radius and nanometer scale IG. As a result, a record high-sensitivity of 563 nm/RIU with a minimum LOD of 3.7×10^{-6} RIU were realized. Concentration sensitivities can reach 981 pm/%, with a minimum concentration detection limit of less than 0.02%. A high resonator Q-factor of 1.6×10^4 accompanied by a low straight single strip waveguide propagation loss of 0.9 dB/cm in the air and 20.2 dB/cm propagation loss of the double slot straight waveguide in the air were achieved in this sensing structure. In comparison to the single strip SOI-based ring resonator sensors reported so far, the sensitivity was more than 2 times that of the specially designed MRRs and the detection range was 3 times larger than that of traditional slot MRRs. Moreover, this is the first fabricated sensor that combines an ultra-compact footprint, ultra-high sensitivity, and ultra-large detection range at the same time. Although the IG-DSMRR was fabricated using EBL, it could also be fabricated using mass production CMOS processes. The IG-DSMRR based on the SOI platform reported here can be applied in numerous chemical, biomedical and environmental applications.

Disclosures. The authors declare no conflict of interest.

Data availability. Data underlying the results presented in this paper are not publicly available at this time but may be obtained from the authors upon reasonable request.

References

1. X. Fan, I. M. White, S. I. Shopova, H. Zhu, J. D. Suter, and Y. Sun, "Sensitive optical biosensors for unlabeled targets: a review," Anal. Chim. Acta **620**(1-2), 8–26 (2008).
2. Q. Xu, D. Fattal, and R.G. Beausoleil, "Silicon microring resonators with 1.5 μm radius," Opt. Express **16**(6), 4309–4315 (2008).
3. D. Dai and S. He, "Highly sensitive sensor based on an ultra-high-Q Mach-Zehnder interferometer coupled microring," J. Opt. Soc. Am. B **26**(3), 511–516 (2009).
4. G. Yuan, L. Gao, Y. Chen, J. Wang, P. Ren, and Z. Wang, "Efficient optical biochemical sensor with slotted Bragg-grating-based Fabry–Perot resonator structure in silicon-on-insulator platform," Opt. Quantum Electron. **47**(2), 247–255 (2015).
5. S. M. Grist, S. A. Schmidt, J. Flueckiger, V. Donzella, W. Shi, S. T. Fard, J. T. Kirk, D. M. Ratner, K. C. Cheung, and L. Chrostowski, "Silicon photonic micro-disk resonators for label-free biosensing," Opt. Express **21**(7), 7994–8006 (2013).
6. I. S. Amiri, M. M. Ariannejad, S. Daud, and P. Yupapin, "High sensitivity temperature sensor silicon-based microring resonator using the broadband input spectrum," Results Phys. **9**, 1578–1584 (2018).

7. E. Luan, H. Shoman, D. M. Ratner, K. C. Cheung, and L. Chrostowski, "Silicon photonic biosensors using label-free detection," Sensors **18**(10), 3519 (2018).

8. S. Schmidt, J. Flueckiger, W. Wu, S. M. Grist, S. T. Fard, V. Donzella, P. Khumwan, E. R. Thompson, Q. Wang, P. Kulik, X. Wang, A. Sherwali, J. Kirk, K. C. Cheung, L. Christowski, and D. Ratner, "Improving the performance of silicon photonic rings, disks, and Bragg gratings for use in label-free biosensing," Biosensing and Nanomedicine VII. SPIE. **9166**, 71–108 (2014).

9. Z. Ruan, L. Shen, S. Zheng, and J. Wang, "Subwavelength grating slot (SWGS) waveguide on silicon platform," Opt. Express **25**(15), 18250–18264 (2017).

10. Q. Huang, K. Ma, and S. He, "FSR-free filter based on a coupled microring grating system," *Optical Fiber Communication Conference* Tu3A.1, 1–3 (2015).

11. A. Arbabi, Y.M. Kang, C. Y. Lu, E. Chow, and L. L. Goddard, "Realization of a narrowband single wavelength microring mirror," Appl. Phys. Lett. **99**(9), 091105 (2011).

12. A. Arbabi, S. M. Kamali, E. Arbabi, B. G. Griffin, and L. L. Goddard, "Grating integrated single mode microring laser," Opt. Express **23**(4), 5335–5347 (2015).

13. X. Cai, J. Wang, M. J. Strain, B. Johnson-Morris, J. Zhu, M. Sorel, J. L. O'Brien, M. G. Thompson, and S. Yu, "Integrated compact optical vortex beam emitters," Science **338**(6105), 363–366 (2012).

14. F. De. Leonardis, C. E. Campanella, B. Troia, A. G. Perri, and V. M. N. Passaro, "Performance of SOI Bragg grating ring resonator for nonlinear sensing applications," Sensors **14**(9), 16017–16034 (2014).

15. C. Y. Chao and L. J. Guo, "Design and optimization of microring resonators in biochemical sensing applications," J. Lightwave Technol. **24**(3), 1395–1402 (2006).

16. J. Wang and D. Dai, "Highly sensitive Si nanaowaire-based optical sensor using a Mach-Zehnder interferometer coupled microring," Opt. Lett. **35**(24), 4229–4231 (2010).

17. V.R. Kolli, T. Srinivasulu, G. Hegde, T. Badrinarayana, and S. Talabattula, "Design and analysis of serially coupled double microring resonator based force sensor for 1 µN range measurement," Optik **131**, 1063–1070 (2017).

18. W. Shi, X. Wang, W. Zhang, H. Yun, C. Lin, L. Chrostowski, and N. A. Jaeger, "Grating-coupled silicon microring resonators," Appl. Phys. Lett. **100**(12), 121118 (2012).

19. T. Ma, L. Sun, J. Yuan, X. Sang, B. Yan, K. Wang, and C. Yu, "Integrated label-free optical biochemical sensor with a large measurement range based on an angular grating-microring resonator," Appl. Opt. **55**(18), 4784–4790 (2016).

20. K. De Vos, I. Bartolozzi, E. Schacht, P. Bienstman, and R. Baets, "Silicon-on-insulator microring resonator for sensitive and label-free biosensing," Opt. Express **15**(12), 7610–7615 (2007).

21. T. Sahba, S. Shon, W. Shi, W. Wu, N. A. F. Jaeger, E. Kwok, D. M. Ratner, and L. Chrostowski, "Optimized sensitivity of silicon-on-insulator (SOI) strip waveguide resonator sensor," Biomed. Opt. Express **8**(2), 500–511 (2017).

22. T. Claes, J. G. Molera, K. De Vos, E. Schacht, R. Baets, and P. Bienstman, "Label-free biosensing with a slot-waveguide-based ring resonator in silicon on insulator," IEEE Photonics J. **1**(3), 197–204 (2009).

23. V. Mere, H. Muthuganesan, Y. Kar, C. V. Kruijsdijk, and S. K. Selvaraja, "On-chip chemical sensing using slot-waveguide-based ring resonator," IEEE Sens. J. **20**(11), 5970–5975 (2020).

24. H. Gu, H. Gong, C. Wang, X. Sun, X. Wang, Y. Yi, C. Chen, F. Wang, and D. Zhang, "Compact inner-wall grating slot microring resonator for label-free sensing," Sensors **19**(22), 5038 (2019).

25. Y. M. Kang, A. Arbabi, and L. L. Goddard, "A microring resonator with an integrated Bragg grating: A compact replacement for a sampled grating distributed Bragg reflector," Opt. Quantum Electron. **41**(9), 689–697 (2009).

26. Achieve More with Light. Available online: http://www.lumerical.com (accessed on 14 November 2019).

27. X. Sang, C. Yu, T. Mayteevarunyoo, K. Wang, Q. Zhang, and P. L. Chu, "Temperature-insensitive chemical sensor based on a fiber Bragg grating," Sens. Actuators, B **120**(2), 754–757 (2007).

28. E. Luan, H. Yun, L. Laplatine, Y. Dattner, D. M. Ratner, K. C. Cheung, and L. Chrostowski, "Enhanced sensitivity of subwavelength multibox waveguide microring resonator label-free biosensors," IEEE J. Sel. Top. Quantum Electron. **25**(3), 1–11 (2018).

29. I. M. White and X. Fan, "On the performance quantification of resonant refractive index sensors," Opt. Express **16**(2), 1020–1028 (2008).

30. S. Hui and H. Xu, "Fresnel-reflection-based fiber sensor for on-line measurement of solute concentration in solutions," Sens. Actuators, B **126**(2), 579–582 (2007).

31. John E. Saunders, Connor Sanders, Hao Chen, and Hans-Peter Loock, "Refractive indices of common solvents and solutions at 1550 nm," Appl. Opt. **55**(4), 947–953 (2016).

32. M. Gnan, S. Thoms, D. S. Macintyre, R. M. De La Rue, and M. Sorel, "Fabrication of low-loss photonic wires in silicon-on-insulator using hydrogen silsesquioxane electron-beam resist," Electron. Lett. **44**(2), 115–116 (2008).

33. K. F. Palmer and D. Williams, "Optical properties of water in the near infrared," J. Opt. Soc. Am. **64**(8), 1107–1110 (1974).

34. C. Ciminelli, F. Dell'Olio, D. Campanella, C.M. , and M. N. Armenise, "High performance SOI microring resonator for biochemical sensing," Opt. Laser Technol. **59**, 60–67 (2014).

35. M. N. Passaro, L. N. Vittorio, and Mario, "Optimizing SOI slot waveguide fabrication tolerances and strip-slot coupling for very efficient optical sensing," Sensors **12**(3), 2436–2455 (2012).

36. T. H. P. Chang, "Proximity effect in electron beam lithography," J. Vac. Sci. Technol. **12**(6), 1271–1275 (1975).